Constraints on Effective Field Theory Couplings Using 311.2 days of LUX Data

D.S. Akerib,[1,2] S. Alsum,[3,*] H.M. Araújo,[4] X. Bai,[5] J. Balajthy,[6] J. Bang,[7] A. Baxter,[8] E.P. Bernard,[9] A. Bernstein,[10] T.P. Biesiadzinski,[1,2] E.M. Boulton,[9,11,12] B. Boxer,[8] P. Brás,[13] S. Burdin,[8] D. Byram,[14,15] M.C. Carmona-Benitez,[16] C. Chan,[7] J.E. Cutter,[6] L. de Viveiros,[16] E. Druszkiewicz,[17] A. Fan,[1,2] S. Fiorucci,[11,7] R.J. Gaitskell,[7] C. Ghag,[18] M.G.D. Gilchriese,[11] C. Gwilliam,[8] C.R. Hall,[19] S.J. Haselschwardt,[20] S.A. Hertel,[21,11] D.P. Hogan,[9] M. Horn,[15,9] D.Q. Huang,[7] C.M. Ignarra,[1,2] R.G. Jacobsen,[9] O. Jahangir,[18] W. Ji,[1,2] K. Kamdin,[9,11] K. Kazkaz,[10] D. Khaitan,[17] E.V. Korolkova,[22] S. Kravitz,[11] V.A. Kudryavtsev,[22] E. Leason,[23] B.G. Lenardo,[6,10] K.T. Lesko,[11] J. Liao,[7] J. Lin,[9] A. Lindote,[13] M.I. Lopes,[13] A. Manalaysay,[11,6] R.L. Mannino,[24,3] N. Marangou,[4] D.N. McKinsey,[9,11] D.-M. Mei,[14] J.A. Morad,[6] A.St.J. Murphy,[23] A. Naylor,[22] C. Nehrkorn,[20] H.N. Nelson,[20] F. Neves,[13] A. Nilima,[23] K.C. Oliver-Mallory,[4,9,11] K.J. Palladino,[3] C. Rhyne,[7] Q. Riffard,[9,11] G.R.C. Rischbieter,[25,†] P. Rossiter,[22] S. Shaw,[20,18] T.A. Shutt,[1,2] C. Silva,[13] M. Solmaz,[20] V.N. Solovov,[13] P. Sorensen,[11] T.J. Sumner,[4] N. Swanson,[7] M. Szydagis,[25] D.J. Taylor,[15] R. Taylor,[4] W.C. Taylor,[7] B.P. Tennyson,[12] P.A. Terman,[24] D.R. Tiedt,[19] W.H. To,[26] L. Tvrznikova,[9,11,12] U. Utku,[18] A. Vacheret,[4] A. Vaitkus,[7] V. Velan,[9] R.C. Webb,[24] J.T. White,[24] T.J. Whitis,[1,2] M.S. Witherell,[11] F.L.H. Wolfs,[17] D. Woodward,[16] X. Xiang,[7] J. Xu,[10] and C. Zhang[14]

(LUX Collaboration)

[1]*SLAC National Accelerator Laboratory, 2575 Sand Hill Road, Menlo Park, CA 94205, USA*
[2]*Kavli Institute for Particle Astrophysics and Cosmology, Stanford University, 452 Lomita Mall, Stanford, CA 94309, USA*
[3]*University of Wisconsin-Madison, Department of Physics, 1150 University Ave., Madison, WI 53706, USA*
[4]*Imperial College London, High Energy Physics, Blackett Laboratory, London SW7 2BZ, United Kingdom*
[5]*South Dakota School of Mines and Technology, 501 East St Joseph St., Rapid City, SD 57701, USA*
[6]*University of California Davis, Department of Physics, One Shields Ave., Davis, CA 95616, USA*
[7]*Brown University, Department of Physics, 182 Hope St., Providence, RI 02912, USA*
[8]*University of Liverpool, Department of Physics, Liverpool L69 7ZE, UK*
[9]*University of California Berkeley, Department of Physics, Berkeley, CA 94720, USA*
[10]*Lawrence Livermore National Laboratory, 7000 East Ave., Livermore, CA 94551, USA*
[11]*Lawrence Berkeley National Laboratory, 1 Cyclotron Rd., Berkeley, CA 94720, USA*
[12]*Yale University, Department of Physics, 217 Prospect St., New Haven, CT 06511, USA*
[13]*LIP-Coimbra, Department of Physics, University of Coimbra, Rua Larga, 3004-516 Coimbra, Portugal*
[14]*University of South Dakota, Department of Physics, 414E Clark St., Vermillion, SD 57069, USA*
[15]*South Dakota Science and Technology Authority, Sanford Underground Research Facility, Lead, SD 57754, USA*
[16]*Pennsylvania State University, Department of Physics, 104 Davey Lab, University Park, PA 16802-6300, USA*
[17]*University of Rochester, Department of Physics and Astronomy, Rochester, NY 14627, USA*
[18]*Department of Physics and Astronomy, University College London, Gower Street, London WC1E 6BT, United Kingdom*
[19]*University of Maryland, Department of Physics, College Park, MD 20742, USA*
[20]*University of California Santa Barbara, Department of Physics, Santa Barbara, CA 93106, USA*
[21]*University of Massachusetts, Amherst Center for Fundamental Interactions and Department of Physics, Amherst, MA 01003-9337 USA*
[22]*University of Sheffield, Department of Physics and Astronomy, Sheffield, S3 7RH, United Kingdom*
[23]*SUPA, School of Physics and Astronomy, University of Edinburgh, Edinburgh EH9 3FD, United Kingdom*
[24]*Texas A & M University, Department of Physics, College Station, TX 77843, USA*
[25]*University at Albany, State University of New York, Department of Physics, 1400 Washington Ave., Albany, NY 12222, USA*
[26]*California State University Stanislaus, Department of Physics, 1 University Circle, Turlock, CA 95382, USA*

(Dated: February 4, 2021)

We report here the results of an Effective Field Theory (EFT) WIMP search analysis using LUX data. We build upon previous LUX analyses by extending the search window to include nuclear recoil energies up to ~180 keV$_{nr}$, requiring a reassessment of data quality cuts and background models. In order to use a binned Profile Likelihood statistical framework, the development of new analysis techniques to account for higher-energy backgrounds was required. With a $3.14{\times}10^4$ kg·day exposure using data collected between 2014 and 2016, we set 90% C.L. exclusion limits on non-relativistic EFT WIMP couplings to neutrons and protons, providing the most stringent constraints on a significant fraction of the possible EFT WIMP interactions. Additionally, we report world-leading exclusion

limits on inelastic EFT WIMP-nucleon recoils.

I. INTRODUCTION

Over the last century, an abundance of evidence suggests that non-baryonic, non-luminous "dark matter" comprises approximately 25% of the universe's energy density [1–5]. A popular dark matter candidate has been the Weakly Interacting Massive Particle (WIMP) with masses between 10 GeV and several TeV [6]. However, non-gravitational interactions with dark matter have never been definitively observed, despite many dedicated experiments over the last several decades.

In an attempt to detect dark matter, the Large Underground Xenon Experiment (LUX) collected data between 2013 and 2016, while being hosted 4850 feet underground in the Davis Cavern at the Sanford Underground Research Facility (SURF) in Lead, South Dakota. The LUX detector was a dual-phase Time Projection Chamber (TPC) equipped with an active xenon mass of 250 kg to detect the possible interactions between WIMP dark matter and Standard Model nucleons. Liquid xenon is a promising target medium for dark matter searches, as they constitute dense, stable targets with well-developed purification techniques. LUX set world-leading limits in the mass range of $\mathcal{O}$(GeV)-$\mathcal{O}$(TeV) for Spin-Independent (SI) WIMP interactions and Spin-Dependent (SD) interactions with neutrons [7–10]. These results were confirmed and improved upon by other Xe TPC-based experiments: XENON1T and PandaX [11, 12].

In this paper, following theoretical work by Fitzpatrick et al. [13] and conventions set by Anand et al. [14], we extend prior analyses by utilizing a generalized Effective Field Theory (EFT) approach going beyond simple SI and SD couplings, with the inclusion of momentum-dependent and velocity-dependent operators. All operators in the WIMP-nucleon interaction, under momentum conservation and Galilean invariance, can be reduced to a basis of four Hermitian quantities:

$$i\frac{\vec{q}}{m_N}, \quad \vec{v}^{\perp} \equiv \vec{v} + \frac{\vec{q}}{2\mu}, \quad \vec{S}_{\chi}, \quad \vec{S}_N \tag{1}$$

where $\vec{q}$ is the momentum transferred from the WIMP to the nucleus, m_N is the nucleon mass, $\vec{v}^{\perp}$ is the component of the relative incoming velocity between the WIMP and the nucleon perpendicular to that momentum transfer, $\vec{S_{\chi}}$ is the spin of the WIMP, and $\vec{S_N}$ the spin of the relevant nucleon.

These quantities are combined into fifteen independent and dimensionless EFT operators:

$$\begin{aligned}
&\mathcal{O}_1 = 1_{\chi} 1_N \\
&\mathcal{O}_2 = \left(v^{\perp}\right)^2 \\
&\mathcal{O}_3 = i\vec{S}_N \cdot \left(\tfrac{\vec{q}}{m_N} \times \vec{v}^{\perp}\right) \\
&\mathcal{O}_4 = \vec{S}_{\chi} \cdot \vec{S}_N \\
&\mathcal{O}_5 = i\vec{S}_{\chi} \cdot \left(\tfrac{\vec{q}}{m_N} \times \vec{v}^{\perp}\right) \\
&\mathcal{O}_6 = \left(\vec{S}_{\chi} \cdot \tfrac{\vec{q}}{m_N}\right)\left(\vec{S}_N \cdot \tfrac{\vec{q}}{m_N}\right) \\
&\mathcal{O}_7 = \vec{S}_N \cdot \vec{v}^{\perp} \\
&\mathcal{O}_8 = \vec{S}_{\chi} \cdot \vec{v}^{\perp} \\
&\mathcal{O}_9 = i\vec{S}_{\chi} \cdot \left(\vec{S}_N \times \tfrac{\vec{q}}{m_N}\right) \\
&\mathcal{O}_{10} = i\vec{S}_N \cdot \tfrac{\vec{q}}{m_N} \\
&\mathcal{O}_{11} = i\vec{S}_{\chi} \cdot \tfrac{\vec{q}}{m_N} \\
&\mathcal{O}_{12} = \vec{S}_{\chi} \cdot \left(\vec{S}_N \times \vec{v}^{\perp}\right) \\
&\mathcal{O}_{13} = i\left(\vec{S}_{\chi} \cdot \vec{v}^{\perp}\right)\left(\vec{S}_N \cdot \tfrac{\vec{q}}{m_N}\right) \\
&\mathcal{O}_{14} = i\left(\vec{S}_{\chi} \cdot \tfrac{\vec{q}}{m_N}\right)\left(\vec{S}_N \cdot \vec{v}^{\perp}\right) \\
&\mathcal{O}_{15} = -\left(\vec{S}_{\chi} \cdot \tfrac{\vec{q}}{m_N}\right)\left(\left(\vec{S}_N \times \vec{v}^{\perp}\right) \cdot \tfrac{\vec{q}}{m_N}\right),
\end{aligned} \tag{2}$$

dividing each $\vec{q}$ by m_N leaves each operator conveniently dimensionless without compromising the operator's hermiticity. We neglect operator $\mathcal{O}_2$ in this analysis, as it cannot arise in non-relativistic scenarios. Each of these operators can in principle be coupled differently to protons versus neutrons (or equivalently, to isoscalars versus isovectors); therefore, we consider 28 different couplings in this analysis. In an actual experiment the dark matter would not couple to an individual nucleon, but to a composite nucleus. This leads to a series of nuclear responses that can vary by target isotope causing certain targets to be better at probing certain operator couplings. Additionally, while the recoil energy spectrum for momentum-independent interactions peaks at zero energy due to kinematics, momentum-dependent operators can have significant contributions at energies well above nuclear recoil energies of 100 keV, motivating analysis of a larger energy window than that used in other LUX analyses [7–10]. Figure 1 shows the differential rate spectra for each of the non-relativistic operators.

A previous EFT analysis was conducted on LUX's first WIMP search (WS) *i.e.* WS2013 [15], consisting of 95 live-days of data collected in 2013. In our current analysis, however, we utilize the longer-duration WS2014–16: 332 live-days collected between 2014 and 2016. We focus solely on WS2014–16 data, as the detector experienced significantly different data-collection conditions between the two science runs, as described in the following section. This creates different systematics and independent analysis frameworks between the two runs, making it difficult to combine both science runs in a single analysis. While a typical WIMP search region is restricted to lower energies, such as ∼40 keV$_{nr}$ in LUX's SI and SD anal-

* salsum@wisc.edu
† grischbieter@albany.edu

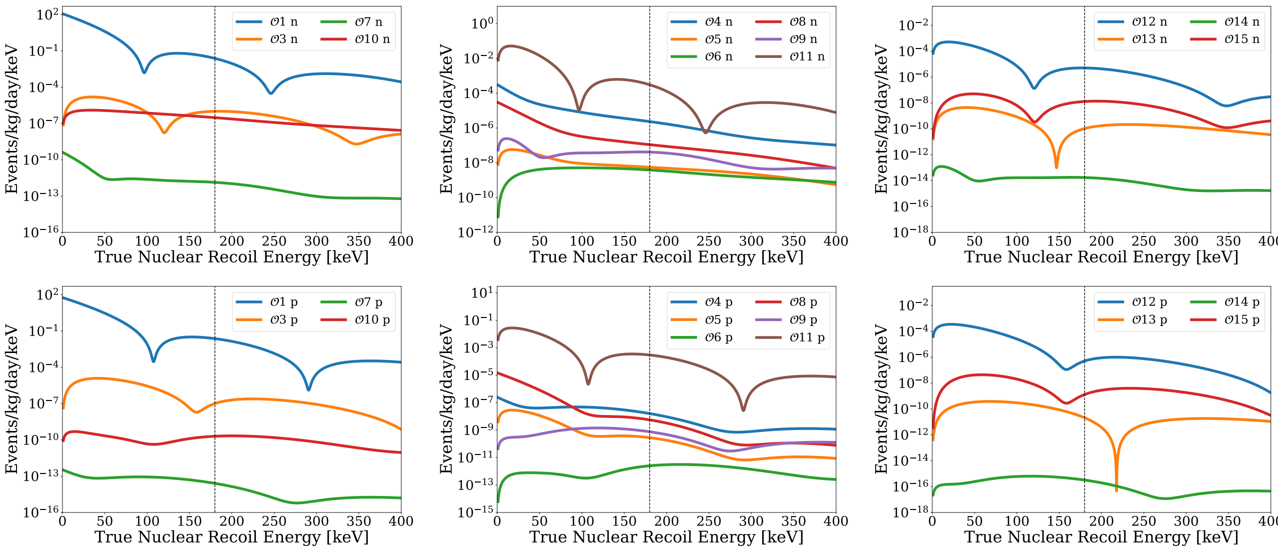

FIG. 1. Differential event rates versus true nuclear recoil energy for the fourteen non-relativistic EFT operators. This example is a 400 GeV WIMP. From left to right: $\vec{S}_\chi$-independent operators, $\vec{S}_\chi$-dependent operators, and $\vec{S}_\chi$-dependent operators that arise only in interactions which do not involve exchange of a spin-0 or spin-1 mediator. Plots on the top row are WIMP-n rates, while the bottom consists of WIMP-p spectra. Vertical dashed black lines correspond to the energy above which the detection efficiency for the analyses presented here falls below 50% (see Fig. 3). For each spectrum, it is assumed that WIMPs only interact with the relevant nucleon through a single operator with the coupling strength set to unity, ignoring the possibility of interference between different operators.

yses [9, 10], this analysis extends the Region of Interest (ROI) to approximately 180 keV$_{nr}$, corresponding to detected scintillation signals (S1) of up to 300 detected photons (phd). As reported in [15], the extension of the WIMP ROI leads to the inclusion of backgrounds considered negligible in the traditional WIMP paradigm. In this work, we describe in detail the necessary steps to take these backgrounds into account.

II. THE LUX EXPERIMENT

As a two-phase TPC utilizing both liquid and gaseous Xe, LUX measures signals by extracting electrons and collecting light released by the Xe target after a recoil event. The initial interaction excites and ionizes electrons from multiple Xe atoms; some ionized electrons recombine with Xe ions, producing additional scintillation light, while others are extracted to the gas layer by an applied electric field where they produce an electroluminesence signal. Initial scintillation light production takes place on timescales of $\mathcal{O}(10$ ns), while the electron drift takes 0–325 μs, creating two distinct signals: S1 and S2, respectively. LUX detected the emitted photons via 122 photomultiplier tubes (PMTs) separated into two arrays at the top and bottom of the detector, with a photon detection efficiency of $\sim$10%. The hit-pattern of S2 light in the top PMT array provides {x,y} coordinate reconstruction of the original event, while the drift time between the S1 and S2 signals provides information regarding event depth.

It is important to note that the amount of primary and secondary scintillation light collected for a given event depends on the location in the detector in which the energy deposition occurred. Because of this, $^{83\mathrm{m}}$Kr dissolved in the LXe (providing a spatially uniform, effectively monoenergetic 41.5 keV electron recoil calibration) was used to construct S1 and S2 detection maps in order to correct for the position-dependence in the observed S1 and S2 signals [16]. This allows us to take advantage of the following linear conversions:

$$S1_c = g_1 \cdot n_\gamma; \qquad S2_c = g_2 \cdot n_e, \tag{3}$$

where $S1_c$ and $S2_c$ are the position-corrected S1 and S2 signals, n_γ and n_e are the initial numbers of photons and electrons leaving the interaction site, and g_1 and g_2 are the scintillation and electroluminescence gains, respectively. We note that while g_1 is simply a geometric light collection efficiency multiplied by PMT quantum efficiency for the prompt scintillation light S1, g_2 is a product of the efficiency to extract electrons from the liquid to gaseous xenon, photons produced per extracted electron in the gas layer, and the S2 photon detection efficiency in the gas [17].

Discrimination between electronic recoil (ER) and nuclear recoil (NR) interactions is possible in a dual-phase xenon TPC, as the total produced quanta, the ratio between excited and ionized electrons for an energy deposition, as well as the recombination probability for ionized electrons, all differ between the two interaction

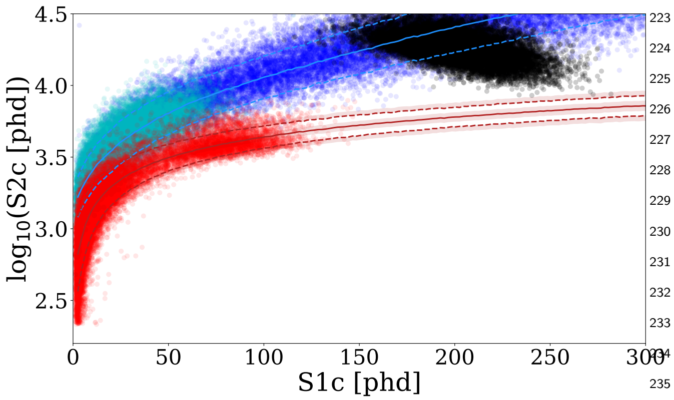

FIG. 2. A sample of single-scatter calibration events taken near the end of WS2014–16 with drift times between 40-105 μs. Cyan points correspond to the ^{3}H β ER calibration; blue points correspond to the ^{14}C β ER calibration; red markers are events associated with the D-D NR calibration; and black markers are $^{83\mathrm{m}}$Kr events. Each population consists of a random selection of 20,000 events. The light blue solid and dashed lines show the expected mean and 90% C.L. ER response region, while red solid and dashed lines show the expected mean and 90% C.L. NR response from NEST v2.1.0. The shaded red region shows the uncertainty in the NR expectation based on *ex situ* NR calibrations reported in the literature (see Sec. IV).

types. However, discrimination is not 100% efficient, as ER events with a stochastically lower charge-to-light ratio can "leak" into the expected NR signal region in {S1, S2} space. As we expect WIMPs to primarily produce NR, it is paramount that we minimize ER leakage, while fully characterizing all backgrounds, in order to distinguish a possible WIMP signal from them.

To characterize the {S1, S2} response of LXe in LUX for both ER and NR interactions, LUX underwent periodic calibrations. For ER, tritiated methane (0–18.6 keV β decay) was injected into the detector several times over LUX's lifetime, providing the LXe response for energies relevant to most typical lower-energy WIMP searches [18]. Additionally, at the end of LUX's tenure in the Davis Cavern, a ^{14}C calibration took place (0–156 keV β decay), allowing for characterization of the ER response out to much higher energies [19]. For NR, an external deuterium-deuterium (D-D) fusion neutron generator was used to provide *in situ* characterization of nuclear recoils between 0.7–74 keV$_{nr}$ [20]. We note here that a nuclear recoil with a given energy produces smaller S1 and S2 signals than an ER event of the same energy; this is due to the fraction of energy from a being transferred to the electrons to produce ionized and excited atoms being smaller for NRs than ERs. Figure 2 shows a sample of the {S1, S2} response for LUX's calibrations compared to expected ER and NR responses from simulation.

Before WS2014–16, LUX underwent a grid conditioning campaign to significantly increase the allowed applied drift field and extraction efficiency. However, this had the unintended consequence of creating a significant amount of trapped charge on the inner walls of the TPC, creating a spatially-distorted and temporally-varying drift field, varying between 50-550 V/cm as function of time and position. 3-D electrostatic models of the built-up charge density were created using the COMSOL Multiphysics software [21], providing a spatial map of the electric field configuration. Field and charge maps were updated monthly, which allows for a robust understanding of the temporal features of the applied drift field. More details are reported in Ref [22]. Additionally, WS2014–16 data were collected with temporally changing gain factors, where g_1 gradually decreased from 0.100$\pm$0.002 to 0.097$\pm$0.001 phd/photon and g_2 varied between 18.9$\pm$0.8 and 19.7$\pm$0.2 phd/e$^-$ [9].

III. DATA SELECTION

For this analysis, data from WS2014–16 are used. Despite the challenges from the temporally varying gain factors (g_1 and g_2) and electric field distortions, WS2014–16 has been well-characterized by multiple analyses since LUX's decommissioning [17, 22, 23]. As the EFT ROI is significantly larger in {S1, S2} space than in the SI and SD WIMP analyses, data quality cuts are crucial for removing backgrounds, including: events with poor position reconstruction; multiple scatters with merged S2 signals; events with gaseous xenon interactions classified as the event's S2; and events with an overabundance of non-S1 and non-S2 pulses such as single photons and electrons not associated with the observed S1 or S2. To minimize potential bias when creating these data quality cuts (described in more detail below), the WS2014–16 data were "salted" with artificial WIMP-like events at early stages of the data-processing pipeline. Details of the salting procedure are described in Ref. [9]. These events are only removed from the data set after all data quality cuts and models (described in Sec. IV) had been finalized. Additionally, energy depositions from LUX's $^{83\mathrm{m}}$Kr calibrations fall into this extended-energy ROI. To combat the additional leakage from the regular high-statistics calibration injections, data acquisition corresponding to significant $^{83\mathrm{m}}$Kr contamination were omitted from this analysis. A similar exclusion was reported in Ref. [24], however, this resulted in a significant loss of live-time. To increase the exposure of this analysis while also maintaining low $^{83\mathrm{m}}$Kr activity, each exclusion period was reduced by 17 $^{83\mathrm{m}}$Kr half-lives (31.1 hours). The final amount of exposure excluded was 20.8 live-days, resulting in a 311.2-day science run.

To account for the temporal and spatial variation of the detector response, the WS2014–16 data are divided into four temporal bins, each further subdivided into four spatial bins corresponding to 65 μs windows of drift time. Selecting periods when the field configuration was approximately static, we approximate each of the resulting 16 bins as temporally static with near-uniform electric field distribution. This results in negligible loss of accuracy for reproduction of light and charge yields. This same division of the data set into 16 date and drift bins was is further described in Refs. [9, 17, 22]. Bins near the bottom of the detector experienced weaker electric fields (50–100 V/cm), while the strongest fields were in the topmost portion of LXe (400–550 V/cm). The four temporal bins result in unequal live times: 43.9, 43.8, 85.8, and 137.7 days. An illustration of the data divided into these 16 time and drift time bins is provided in Appendix A.

The fiducial volume is defined as the region for which the elcetron drift time (vertical coordinate) lies between 40 and 300 μs and (in the radial dimension) the region that is greater than 3 cm inward from the TPC wall. The distorted electric field also caused the electron drift paths to bend significantly inward as the electrons drift from the interaction vertex to the liquid surface. This effect is strongest for events originating near the bottom of the TPC. As a result, near-wall events at the bottom of the TPC have more centralized S2 hit-patterns in the top PMT array than near-wall events at the top of the TPC. Effectively, this moves the observed wall position inward at the bottom of the TPC, requiring that the fiducial LXe target volume is reduced as a function of drift time. In temporal order, the resultant fiducial masses for each WS2014–16 date bin are: 105.4±5.3, 107.2±5.4, 99.2±5.0, and 98.4±4.9 kg. These volumes are determined by counting remaining $^{83\mathrm{m}}$Kr events after applying fiducial cuts, and using the knowledge that the full TPC volume contains 250 kg of LXe. The total exposure used in this analysis therefore is $3.14{\times}10^4$ kg·days.

To remove adverse events that are would be incorrectly classified as single scatters from the data set, a series of data quality cuts are applied. Events with an overabundance of pulses preceding or following either the S1 or S2 — such as single photons or single electrons emitted from the detector's grids or delayed releases from impurities [25] — were removed, as these events are more likely to have misidentified S1 or S2 signals. Cuts are applied based on the S1 PMT hit-patterns as well as the shape of the S1 pulse; these remove events where S1s may originate from light leaking in from outside the TPC walls and misidentified S1s, respectively. For S2s, cuts are applied based on the pulse width and shape as a function of area and drift time. As bulk S2s are expected to be approximately Gaussian in shape [26], a cut on the goodness of a Gaussian fit to the pulse shape was implemented. The mean single-scatter selection efficiency of these cuts based on ER and NR calibration data and simulations is 96% between 0-300 phd, while the full NR detection efficiency is shown in Figure 3.

Unmodeled backgrounds in and below the signal region were reported in Ref [15]. There is a 5.6 cm gap between the cathode and the bottom PMT array; scintillation produced in this region is visible to the PMTs, but emitted electrons are carried downward (instead of upward to produce an S2 signal). If a γ-ray scatters in this sub-cathode region in addition to the fiducial volume, both scatters contribute to the S1, while only the fiducial scatter produces S2 light. The result is a "$\gamma - X$" event with an S1–S2 ratio anomalously low for an ER event. Combined with the reduced recombination due to having the weakest electric fields at the bottom of the fiducial region, these events could significantly increase the leakage of ER events into the NR signal region.

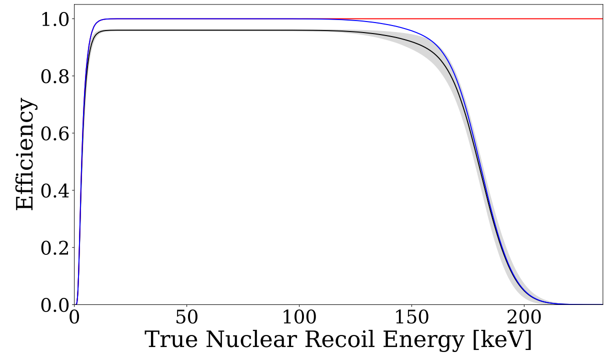

FIG. 3. Nuclear Recoil detection and selection efficiencies based on calibration data and simulations. Red corresponds to S1+S2 detection efficiency in the fiducial target without any data selection cuts applied, while blue corresponds to the mean detection efficiency in the EFT {S1, S2} ROI. The black curve corresponds to the mean overall efficiency after data quality cuts are applied, and the grey band signifies the standard deviation of the efficiency due to differing temporal and spatial detector conditions.

$\gamma - X$ events pose a unique challenge because they can appear as typical single scatters. Any hints of their anomalous behavior could in principle be captured in the S1 signal. However, due to the timescales at which light collection takes place ($\mathcal{O}(10$ ns$)$) being longer than transit time between scatters (typically less than 1 ns), these S1s are not separable from single scatters using simple shape cuts, such as those described above. Instead, a six-dimensional parameter space is utilized, with the intent of using a Boosted Decision Tree (BDT) machine learning event classifier to identify and remove $\gamma - X$-like events. BDTs are becoming more commonly used in particle physics analyses, and they provide an efficient way to draw distinctions between two populations in higher-dimensionality phase spaces [26, 27]. The six features used are: $S1c$; $S2c$; electron drift time; the mean size of the hit pattern in the bottom PMT array, or "cluster" size; the fraction of the total S1 light detected by the PMT registering the largest contribution to the S1; and the ratio of collected scintillation light in the top and bottom PMT arrays. By utilizing information from S1 hit-patterns in the bottom PMT array with position reconstruction information from the S2, we hope to separate $\gamma - X$ events from true single scatters. To train the $\gamma - X$ classifier, a model was made by characterizing double-scattering events near the cathode but using simulation to extrapolate these double scatters into $\gamma - X$ events with a sub-cathode energy deposit. More details of the $\gamma - X$ model are discussed in Sec IV.

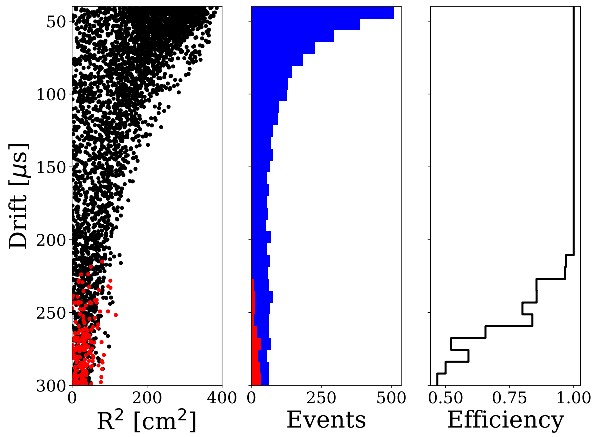

FIG. 4. *Left*: Spatial distribution of the background data. Red markers correspond to events removed by the BDT $\gamma-X$ cut. *Center*: Histograms of events as a function of detector depth. Blue corresponds to all events, while red corresponds to the events removed with application of the BDT cut. *Right*: Efficiency as a function of event depth. While the efficiency is the poorest near the bottom of the detector, the background data are mostly concentrated near the top, resulting in a 99.2% overall efficiency from the BDT cut for the background data.

The cut using the trained BDT rejects 89.2% of simulated $\gamma-X$ events, while only removing 1.7% of simulated single scatters, reducing our signal detection efficiency to 94.4%. The efficiency is highly position-dependent, with 100% efficiency throughout most of the volume, but the largest loss of efficiency in the bottom-most 20% of the fiducial target (near 50% at the poorest). Figure 4 details the $\gamma - X$ cut efficiency in the background data.

IV. MODELING

Using the Profile Likelihood Ratio (PLR) construction (described in Sec. V), we use statistical inference to quantify the level of sensitivity of our detector to identify or constrain the possibility of WIMPs interacting under a given EFT operator. A likelihood ratio test provides a strong statistical framework when dealing with higher-dimensionality parameter space, and it requires a good model of both the null and alternative hypotheses to be valid. In this section, we describe the construction of each of the models used in the PLR framework. We identified and constructed five-dimensional models ($S1_c$, $S2_c$, radius, drift time (d), and azimuthal angle (ϕ) about the TPC's central axis) for the sources that could lead to events in our ROI: EFT WIMPs; ER single scatters; remaining $^{83\text{m}}$Kr after the calibration injections; degraded events and ion recoils from the TPC walls; $\gamma - X$; and accidental coincidences of unrelated S1-only or S2-only events. After separation of the data into the 16 date and drift time bins, we make the assumption that the field variation in each drift time bin has minimal impact on the S1 and S2 distributions. Accordingly, we make the simplification of separating the spatial and energetic components of most models, resulting in Probability Density Functions (PDFs) that are the direct product of two ($S1_c$ and $S2_c$) and three (r, ϕ, and d) dimensions. However, the model for degraded wall events and ions has no such separation as the energy and spatial observables are highly correlated even after separation into 16 drift time bins (see Sec. IV D).

A. Signal Modeling

Signal spectra are obtained using the Mathematica package developed by Anand et al. [14]. This gives the differential rate of nuclear recoils per recoil energy, E_R:

$$\frac{\mathrm{d}R}{\mathrm{d}E_R} = N_T \frac{\rho_0 m_N^2}{2\pi m_\chi m_A} \int_{v>v_{\min}} \frac{f(\vec{v})}{v} |\mathcal{M}|^2 \, \mathrm{d}^3 v, \tag{4}$$

where N_T is the number of target nuclei, ρ_0 is the local dark matter density, m_χ is the mass of a WIMP, m_A is the target nucleus mass, and $f(\vec{v})$ is the galactic WIMP velocity distribution for which we assume a Maxwell-Boltzmann distribution following the Standard Halo Model: characteristic velocity $v_0 = 220$ km/s and escape velocity $v_{esc} = 544$ km/s. The spin-averaged matrix element $|\mathcal{M}|^2$ is calculated via a combination of WIMP velocity and momentum-transfer dependent form factors $F_{ij}^{(N,N')}\left(v^2, q^2\right)$ presented in Appendix A.2 of [13], scaled based on the value of the EFT coupling constants $c_i^{(N)}$:

$$\begin{aligned} &\frac{1}{2j_\chi + 1} \frac{1}{2j+1} \sum_{\text{spins}} |\mathcal{M}|^2 \equiv \\ &\frac{m_A^2}{m_N^2} \sum_{i,j=1}^{15} \sum_{N,N'=p,n} c_i^{(N)} c_j^{(N')} F_{ij}^{(N,N')}\left(v^2, q^2\right), \end{aligned} \tag{5}$$

where j and j_χ are the spins of the nucleus and WIMP, respectively. Note that this representation of the amplitude differs from Ref [13] by a factor of $(4 m_\chi m_N)^2$, accounting for the different normalization conventions and dimensionality of the c_i used in the Mathematica package [14]. The form factors are also affected by differing conventions and are scaled to account for this[1]. Putting equations 4 and 5 together, the differential rate spectrum becomes

$$\begin{aligned} \frac{dR}{dE_R} = N_T \frac{\rho_0 m_A}{2\pi m_\chi} \int_{v>v_{min}} \Bigg[&\frac{f(v)}{v} \\ &\cdot \sum_{i,j} \sum_{N,N'=n,p} c_i^N c_j^{N'} F_{i,j}^{(N,N')}\left(v^2, q^2\right) \mathrm{d}v \Bigg]. \end{aligned} \tag{6}$$

[1] Specifically, factors of factors of $\vec{q}$ have been normalized by factors of m_N, similar to the normalization used in Equations 1 and 2.

Note that one can just as easily use isoscalars and isovectors in place of the p and n for the proton and neutron. This is also a valid approach, and has been done in analyses by several other experiments as it allows for direct comparisons between experiments with different target compositions [28–30]. However, the $\{n,p\}$ basis is used in this analysis, as it provides a more natural representation of the physical interactions that this analysis attempts to identify or constrain. Additionally, due to the presence of two couplings in each term, the possibility for destructive interference exists. For this analysis, we ignore the possibility of interference and make the assumption that one coupling is dominant over all others. As such, the signal spectra that we obtain are the result of setting all but one of the couplings $c_i^{(N)}$ to 0. The resulting differential event rate scales linearly with the remaining non-zero coupling $c_i^{(N)^2}$:

$$\frac{dR}{dE_R} = N_T \frac{\rho_0 m_A}{2\pi m_\chi} \int_{v>v_{min}} \frac{f(v)}{v} c_i^{(N)^2} F_{i,i}^{(N,N)}\left(v^2, q^2\right) \mathrm{d}v, \qquad (7)$$

Due to the linear relation between differential rate and $c_i^{(N)^2}$, the spectrum for any value of the coupling constant can be easily determined by calculating the $c_i^{(N)^2} = m_v^{-2}$ case and then scaling appropriately. We use the benchmark value m_v^{-2}, where $m_v = 246.2$ GeV and is the Higg's vacuum expectation value, as this is the chosen scaling factor used internally by [14].

To generate the detector response to the resultant nuclear recoil energy spectra, a recent release of the Noble Element Simulation Technique (NEST v2.1.0) was utilized [31], chosen prior to unsalting. An empirical fit to all existing nuclear recoil data in LXe, NEST provides precise light and charge yields resulting from an energy deposition. While the D-D NR calibrations characterize the detector response out to 74 keV$_{nr}$ (∼150 phd), NEST allows for extrapolation to higher energies using reported yields in the literature extending to 330 keV$_{nr}$ from other sources such as AmBe [32]. This provides an understanding of the signal region beyond where the detector NR response was directly calibrated. Uncertainty in the signal region for energies beyond the *in situ* D-D calibration was calculated by allowing the NEST v2.1.0 NR model (largely unchanged between versions 2.0.1 through 2.2) to fluctuate within the uncertainties for the total reported quanta of the highest energy data used to fit the model; for 300 phd S1s, the resultant uncertainty of the location of the NR band mean in S2-space is approximately 7.5%, corresponding to a change in S2 size of roughly 540 phd. Ultimately, the NR band is sufficiently far from the ER band in any scenario to make this difference negligible.

Recoil spectra for different operator-mass combinations are simulated using the LUX Legacy Analysis Monte Carlo Application (LLAMA) [17]. LLAMA uses spatial and temporal interpolation between the 16 approximately-static WS2014–16 drift time bins, utilizing the NR response from NESTv2.1.0 and the three-dimensional field maps described in Ref. [22]. Signal spectra are generated homogeneously throughout the detector.

Generation of the inelastic EFT WIMP-nucleon signal models used recoil spectra from a modified version of the Anand et al. Mathematica package developed by Barello et al. [33]. This version introduces an additional energy conservation requirement,

$$\delta_m + \vec{v}\cdot\vec{q} + \frac{|\vec{q}|^2}{2\mu_N} = 0, \qquad (8)$$

where δ_m is the mass splitting term between the incoming and outgoing WIMP ($\delta_m = m_{\chi_2} - m_{\chi_1}$). This requirement is included into our basis of Hermition quantities by an additional term in the perpendicular velocity proportional to δ_m,

$$\vec{v}_{inel}^{\perp} \equiv \vec{v} + \frac{\vec{q}}{2\mu} + \frac{\delta_m}{|\vec{q}|^2}\vec{q} = v^{\perp} + \frac{\delta_m}{|\vec{q}|^2}\vec{q}. \qquad (9)$$

Signal models with a range of δ_m from 0–200 keV were generated for all operators in the isoscalar basis using a WIMP mass of 1 TeV/c^2. Other parameters, including astrophysical and nuclear, remain unaltered from those used for the elastic signal models, and the same procedure was applied.

B. Standard ER Backgrounds

We expect the overwhelming majority of backgrounds to originate from ER-producing contaminants within the LXe, namely ^{222}Rn and ^{220}Rn and their charged daughter isotopes plating-out on the detector surfaces, as well as decays from radioisotopes in the detector components. Decays from the detector components are mostly isotopes originating from ^{238}U, ^{232}Th, ^{60}Co, and ^{40}K, producing β, γ, and α radiation at a wide range of energies. A dedicated modeling campaign for reproducing the LXe ER response in LUX was reported in Ref. [17]. To summarize, utilization and tuning of NEST ER response models allowed for accurate characterization of the temporal and spatial features of the WS2014–16 detector, and precise reproduction of all available LUX ^{14}C and CH_3T ER calibration data. While NEST is a global fit to xenon light and charge yields, this LUX-specific version allows for efficient creation of high-statistics LUX ER simulated data for all 16 WS2014–16 drift and date bins for all relevant energies.

Assays of LUX components provide initial expectations for the expected radioactivity from the detector leading to ER backgrounds. However, due to uncertainties in the assay measurements and the modeled response of each detector component and their geometries, the simulated energy depositions from each contributing detector component and radiogenic source was fit to high-energy data, including multiply-scattering events, allowing for effective activities from each source. Data below 80 keV were excluded when fitting the effective activities. LXe light and charge responses for each source were then simulated using the LUX-specific version of NESTv2.1.0, providing $S1_c$ and $S2_c$ distributions for each expected ER source.

C. The $^{83\mathrm{m}}$Kr Model

$^{83\mathrm{m}}$Kr was injected into the TPC on a weekly basis to ensure proper position corrections. This source decays in two transitions: 32.1 keV followed by 9.4 keV. Most often, these de-excitations occur via internal conversion electrons or Auger electrons. The time between the two emissions ranges from $\mathcal{O}(10$ ns) to $\mathcal{O}(1$ μs), and those on shorter timescales appear as 41.5 keV single scatters, having only a single detectable S1 and S2. These quasi-monoenergetic depositions are of high enough energy to be cut from a typical momentum-independent analysis, leading to no loss of exposure time. However, in an analysis reaching to higher energies, $^{83\mathrm{m}}$Kr events can interfere with the signal region.

As a high-statistics monoenergetic peak, $^{83\mathrm{m}}$Kr yields are observed with wide recombination fluctuations in the $\frac{S2}{S1}$ ratio, resulting in events near the NR signal region at energies where most other ER backgrounds are well-discriminated (see Fig. 2). Additionally, this proximity of $^{83\mathrm{m}}$Kr events to the signal region worsens for weaker fields, as the ER and NR bands are less separated than at stronger electric fields. As stated in the Sec. III, 20.8 live-days were excluded from WS2014–16 that correspond to periods of significant $^{83\mathrm{m}}$Kr contamination in order to omit most of these events from this analysis.

Despite this, some $^{83\mathrm{m}}$Kr events are expected in the data set; $^{83\mathrm{m}}$Kr has a 1.83 hour half-life, resulting in lingering decays after the injections end. Therefore, a robust characterization of these events was required. For this, the remaining $^{83\mathrm{m}}$Kr data excluded from the final search data were used to construct a model for these events. The expected number of events was calculated by measuring the rate of $^{83\mathrm{m}}$Kr events at the end of each data exclusion period and extrapolating using the known half-life.

D. The Wall Model

Similarly to previous LUX analyses [9, 34], we construct a model characterizing energy depositions in close proximity to the inner TPC walls. The electron extraction efficiency near the walls is poorer than in the bulk LXe, resulting in degraded S2 signals. Additionally, nuclear recoils from ^{206}Pb (a daughter of ^{210}Po α-decay) on the inner TPC walls leads to events with naturally low $\frac{S2}{S1}$ ratios compared to ER backgrounds, resulting in a population of events well-below the signal region in $\{S1_c, S2_c\}$ space.

As mentioned briefly at the beginning of this section, the reconstructed position of the detector wall depends on the drift time d, azimuthal angle ϕ, and acquisition time [22] due to the radial field. We observed that the reconstructed position of the events fluctuates around the position of the wall according to a Gaussian distribution with width proportional to $1/\sqrt{S2_{raw}}$ [35]. Therefore, the wall events have a larger uncertainty for the same deposited energy due to the smaller S2 size, allowing for a fraction of these events to appear within the fiducial volume.

To characterize this background, we selected WS2014–16 events with reconstructed positions beyond the measured position of the TPC wall, counting the number of events for a specific bin in drift time, azimuth, and acquisition time, as the fluctuations in reconstructed position about the wall should be equal both inside and outside the wall position. Integrating the tail of this empirical fit provides an understanding of the expected number of wall events that leak into the fiducial volume. Since this leakage depends heavily on the observed S2 size, the energy and spatial PDFs are significantly correlated, making the wall model a true five-dimensional PDF.

E. The $\gamma - X$ model

As described in Sec. III, we consider the possibility of multiply-scattering γ-rays with only a single detectable ionization signal due to one or more sub-cathode energy depositions: $\gamma - X$. With only a single S2, these events appear as single scatters, as the individual energy depositions occur at short-enough timescales where the primary scintillation from each interaction blends into a single S1 signal. However, the detected S2 corresponds to only a fraction of the recoil energy that corresponds to the S1. This creates the possibility of ER events having observed $\frac{S2}{S1}$ ratios similar to nuclear recoils. These events would be observed near the bottom of the fiducial volume, where the electric field values are the weakest and the ER/NR discrimination is the poorest, creating the possibility of excessive ER leakage.

The volume of LXe between the cathode and bottom PMT array is referred to as the "Reverse Field Region" (RFR), where the mean applied electric field is anti-parallel to the above-cathode region, causing electrons to drift downwards away from the extraction region. Gammas coming from radiogenic impurities in the bottom PMT array and RFR TPC walls – namely ^{238}U, ^{232}Th, ^{60}Co, ^{40}K and their daughters – may deposit energy in the RFR before scattering in the fiducial target. Additionally, back-scattering events originating from the cathode grid wires can also contribute to the $\gamma - X$ rate. The RFR field magnitude is of $\mathcal{O}(1$ kV/cm), which results in significantly lower light yields for a given energy deposition compared to the bottom of fiducial volume: a reduction to 75% for 50 keV γ-rays [31]. This results in higher-energy γ-rays (which are more likely to traverse a significant portion of the RFR xenon) producing S1s below our 300 phd threshold that would normally be excluded if that interaction occurred in the bulk LXe. These events become more likely as the search window extends to higher energies, as multiply-scattering γ backgrounds become more prevalent. Therefore, characterizing and modeling these events becomes necessary for an analysis with an extended-energy ROI.

Because $\gamma - X$ events appear superficially as normal single scatters, we are unable to obtain a data set of known $\gamma - X$ events. However, the presence of double-scatter events near the cathode provides information on multiply-scattering γ-rays near the RFR. We selected a set of double-scatter events that had: at least 3 cm of vertical separation between the two reconstructed interaction locations; $S1_c$ less than 300 phd; the lower-most S2 within 4 cm of the cathode; and the top-most energy deposit within the fiducial radius. The distance between the cathode and the fiducial volume is approximately 3 cm, thus the first condition reproduces the minimum vertex separation for $\gamma - X$ events that may pass other data quality cuts. The remaining criteria allow for selection of events with uppermost S2s similar to single scatters in the background data (as those would be the observed S2s for $\gamma - X$ events). Seventeen of these "near-miss" double-scatters were found in WS2014–16, and a model was created that replicated the behavior of these near-miss events using the LUX-specific NEST framework. By translating this model 4 cm downwards, guaranteeing the first simulated scatter to be sub-cathode, we were able to generate simulated $\gamma - X$ events based on LUX data. Additionally, this model was used to train the BDT described in Sec. III in an attempt to remove most $\gamma - X$ events in the data. While characterizing the rate of expected $\gamma - X$ events proves challenging, we make the assumption that it should be similar to the rate of near-miss double-scatter events. Taking the efficiency of the BDT cut into account with respect to simulated $\gamma - X$, we therefore expect $\mathcal{O}(1)$ $\gamma - X$ events.

F. Accidental Coincidences

Lastly, we take into consideration the coincidental pairing of unrelated S1-only and S2-only events, forming an "accidental" single scatter (such as those reported in Ref. [36]). To understand the rate at which to expect these events and their appearance in phase space, LUX data were filtered to obtain two sets of data: events with only one observed S1 and no S2, and events with only one S2 and no S1. The S1-only and S2-only rates and spectra were input into a Monte Carlo generator, and random pairing of S1s and S2s provided a model to characterize these events.

It is possible to have energetic S1-only and S2-only events due to energy depositions in regions of poor light collection and charge extraction efficiencies; however, the most common S1-only and S2-only events consist of only a handful of photons or electrons, respectively. The accidental pairing of these pulses can produce a false event mimicking a lower-energy single scatter, falling in the region of phase space where the expected WIMP recoil rate is the most probable. Using the S1-only and S2-only event rates, we are able to calculate an expectation for accidental coincidence events. However, the data quality cuts described in Sec. III reduce the expected rate of these events in the ROI considerably, and we expect less than a single accidental event for the exposure in this analysis.

V. STATISTICAL METHODOLOGY

In setting constraints on the coupling constant for a given mass-operator combination, we use hypothesis test inversion to determine a 2-sided frequentist confidence interval via the Neyman Construction [37]. This involves performing a series of hypothesis tests where the null hypothesis (H_0) is our model with the Parameter Of Interest (POI), μ, fixed at a given value, and the alternative hypothesis (H_1) is allowed to float to all real values:

$$\begin{aligned} \mathrm{H}_0 &: \mu = \mu_0 \\ \mathrm{H}_1 &: \mu \neq \mu_0 \end{aligned} \tag{10}$$

Here, μ is simply the number of WIMP-nucleon scatters we expect to observe for a given model. The values of the POI corresponding to hypothesis tests whose p-value is greater than the significance $\alpha = 0.1$ form the 90% confidence interval on the POI for each signal model.

Our test statistic for these hypothesis tests is the Profile Likelihood Ratio (PLR). More specifically, we use the negative log likelihood, $q = -2\ln(\lambda)$, where λ is the actual PLR:

$$\lambda(\vec{X}) = \frac{\mathcal{L}_P\left((\mu_0, \hat{\hat{\theta}})\middle|\vec{X}\right)}{\mathcal{L}_P\left((\hat{\mu}, \hat{\theta})\middle|\vec{X}\right)}. \tag{11}$$

Here, P denotes that this likelihood has been modified by the presence of a profile. μ_0 is just the fixed POI, and the terms with hats are allowed to float to maximize the value of the profiled likelihood $\mathcal{L}_P$. The double hat $\hat{\hat{\theta}}$ indicates that the values of the nuisance parameters, θ, that maximize the likelihood in the case of $\mu = \mu_0$ are not in general the same values that maximize it when μ is left to float. $\vec{X}$ represents the data set used to compare against the model.

For this analysis we use the extended unbinned likelihood as follows:

$$\begin{aligned}\mathcal{L}\left(\left(\mu,\vec{\theta}\right)\middle|\vec{X}\right) &= \mathrm{Pois}\left(n_{\mathrm{obs}};n_{\mathrm{exp}}\right)\\ &\cdot\prod_{\vec{x}_i\in\vec{X}}\Bigg[n_{\mathrm{sig}}R_{\mathrm{sig},t_i,z_i}\mathcal{P}_{\mathrm{sig},t_i,z_i}\left(\vec{\mathcal{O}}_i\right)\\ &\quad+\sum_{b_j}n_{b_j}R_{b_j,t_i,z_i}\mathcal{P}_{b_j,t_i,z_i}\left(\vec{\mathcal{O}}_i\right)\\ &\quad+n_{\mathrm{wall}}R_{\mathrm{wall},t_i,z_i}\mathcal{P}_{\mathrm{wall},t_i,z_i}\left(\vec{\mathcal{O}}_i\right)\Bigg]\\ &\cdot\prod_{\theta_i\in\vec{\theta}}\mathcal{P}_i\left(\theta_i\right)\end{aligned} \quad (12)$$

Here n_{obs} is the number of events contained in the data set, $\vec{X}$; $n_{\mathrm{exp}} = n_{\mathrm{sig}} + \sum_{b_i} n_{b_i} + n_{\mathrm{wall}}$ is the number of events expected by the model with b_i indicating one of our background models; and $\vec{x}_i$ is a given data point in the set $\vec{X}$. Each data point $\vec{x}_i$ contains the set of 5 observables: $\{r, d, \phi, S1_c, \text{ and } S2_c\} \equiv \vec{\mathcal{O}}$ along with the analysis bin in which it was measured: $\{\text{date bin}(t), \text{drift time bin}(z)\}$. n_{sig} is the number of signal events expected, and is used as a stand-in for our POI as we have not included any nuisance parameters that affect detector thresholds in this analysis, thus n_{sig} is a function purely of $c_i^{(N)^2}$. n_{b_i} is similarly the number of expected events from background source b_i, and the same is true of n_{wall}. $R_{\mathrm{source}}, t_i, z_i$ is the fraction of the total number of expected events for that source that are expected to occur in the bin (date bin $= t_i$, drift time bin $= z_i$). Likewise, $\mathcal{P}_{\mathrm{source}}, t_i, z_i\left(\vec{\mathcal{O}}_i\right)$ is the Probability Density Function (PDF) modeled for the given source in the given date bin and drift time bin. The final line in equation 12 is the profile term. θ_i is a given nuisance parameter, and $\mathcal{P}_i(\theta_i)$ is the PDF describing the profile for that nuisance parameter. In principle, the profiles of multiple nuisance parameters could be correlated, but this was determined to have minimal effect and was not implemented. The set of nuisance parameters $\vec{\theta}$ used in this analysis is simply the number of expected events for each different background source n_{b_i}.

We explicitly separate the wall model from the other backgrounds in Eqn. 12 because its implementation in our software differs significantly from the others. As mentioned in Sec. IV, the spatial observables $\{r, d, \phi\}$ were determined to be sufficiently independent of the corrected energy observables, $\{S1_c, S2_c\}$, once the detector was split up into its date bins and drift time bins. This allowed for the implementation of the 5-dimensional PDF to be split into the direct product

$$\begin{aligned}\mathcal{P}_{\mathrm{source},t_i,z_i}\left(\vec{\mathcal{O}}_i\right) &\equiv \mathcal{P}_{\mathrm{source},t_i,z_i}\left(r_i,d_i,\phi_i\right)\\ &\cdot\mathcal{P}_{\mathrm{source},t_i,z_i}\left(S1_{c,i},S2_{c,i}\right)\end{aligned} \quad (13)$$

However, in the case of the wall model, this split is not feasible: the location of the wall as seen by the top PMT array depends significantly on d and ϕ, while the reconstructed distance from the wall depends strongly on $S2_c$. Therefore, the PDFs for the wall model remain fully 5-dimensional.

We found that our data sets do not lie in the asymptotic regime, and therefore unfortunately cannot make use of the asymptotic formulae that would greatly reduce the computation necessary for performing each hypothesis test [38]. Instead, we rely on comparing our test statistic to that of a collection of Monte Carlo psuedoexperiments simulated based on our models. Test statistic distributions are evaluated using a custom-built PLR framework utilizing RooFit [39] that has been optimized for the rapid computation of psuedoexperiments in our 5-dimensional regime.

VI. RESULTS

Figure 5 shows the final WS2014–16 data used in this analysis, with the events used in the PLR framework highlighting the behavior of the different background models. The max ROI is the region of $\{S1_c, S2_c\}$ space that includes at least 90% of the expected differential rate from each signal model. The initial constraints and final fits for each nuisance parameter are shown in Table I, where fit values are for the background-only scenario. We set a 2-sided frequentist confidence interval on the value of $c_i^{(N)^2}$ using the method discussed in Sec. V at a 90% confidence level ($\alpha = 0.1$). We do this for all operators, selecting values for the WIMP mass ranging from 10 GeV to 4 TeV. Upper-limits are shown in Fig. 6 and Fig. 7 for WIMP-neutron and WIMP-proton interactions, respectively. We explicitly note here that the $c_i^{(N)}$ have dimensionality of $[\mathrm{mass}]^{-2}$ as the conventions of Ref. [14] use a dimensionless operator representation and normalize spinors to unity, which differs from the representation used in Ref. [13]. Consequently, results are scaled by a factor of m_v^2 in order to report dimensionless values similar to the results reported in Ref. [29] for convenience. Figures 6 and 7 additionally show the available comparisons with the upper-limits from the 1.4×10^4 kg·day exposure results using LUX WS2013 data [15].

Our data set shows consistency with our background models, resulting in p-values between 0.14 and 0.50 for the 28 operator/nucleon combinations at 50 GeV mass, with a median p-value of 0.28. Additionally, Kolmogorov-Smirnov tests for each of the five observables – $S1_c$, $S2_c$, r, d, and ϕ – compared to the background model PDFs return p-values: 0.39, 0.24, 0.60, 0.43, and 0.81, respectively. However, due to the presence of observed data in regions of phase space where our background models and signal models overlap, the upper-limits on the number of WIMP scatters are greater than the expectation for certain signal models. These data include low-energy accidental-like events, a handful of $\gamma - X$-like events near the bottom of the fiducial volume, and $^{83\mathrm{m}}$Kr events from the lowest drift time bin. While

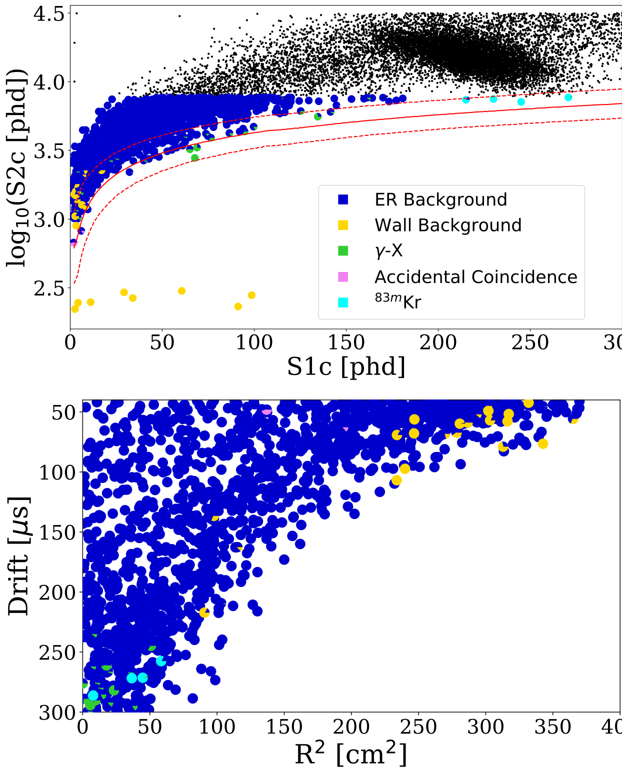

FIG. 5. The final unsalted WS2014–16 data used in this analysis. Black markers indicate that the event was outside the final ROI used by the PLR. The remaining data are colored to indicate the values of a given model PDF at that point in phase space. Data can have multi-colored markers, indicating that our expected background models overlap in certain regions of phase space. Note that all 16 drift time bins are merged in this plot, and the red solid and dashed lines represent the mean and 90% C.L. expected NR signal response averaged over the 16 drift time bins. *Top*: Distribution of events in {S1, S2} space. *Bottom*: Spatial distribution of final events using radii as seen by the top PMT array and electron drift time. Note that the spatial distribution is not constant as a function of ϕ.

these events are included in our background model, uncertainties in their expected rates leads to allowed signal events from several EFT WIMP models. This results in weaker sensitivity limits for several combinations of operator and mass when compared to the background-only expectation. Most operators remain within 2σ of our expectation, with the exception of $\mathcal{O}_{13}$ and $\mathcal{O}_{15}$, which differ from the expected sensitivity by as much as 2.8σ. This is understood by referencing Fig. 1; the operator models that produce our weakest limits are those with the lowest expected differential rate at both the highest and lowest energies in our ROI and are relatively flat at intermediate energies (see $\mathcal{O}_3$, $\mathcal{O}_{13}$, and $\mathcal{O}_{15}$ and compare to Figures 6 and 7). When compared to our data (Figure 5), the events that are not inconsistent with the signal models follow this trend, where most of our observed background leakage occurs at the intermediate energies of our ROI.

TABLE I. The nuisance parameters used in the PLR framework, along with their initial constraints and fit values.

Parameter	Constraint	Fit Value
Standard ER	1498.0±187.5	1495.1±51.2
Wall-based Backgrounds	11.3±2.8	12.8±2.2
$\gamma - X$	3.4±2.5	5.2±2.0
$^{83\text{m}}$Kr	5.2±1.5	4.8±1.3
Accidental Coincidence	$0.41^{+0.43}_{-0.41}$	0.51±0.39

Figure 9 in Appendix A shows the data separated into the individual 16 drift and date bins, providing a qualitative characterization of the ER encroachment upon the signal region.

Despite the resultant limits being slightly poorer than our expectation, these are leading limits for several operators in various regions of parameter space using the $\{n,p\}$ basis, as opposed to {isoscalar,isovector}. Other reported $\{n,p\}$ limits in the literature were set using significantly less exposure than this analysis [15, 40]. Recent competitive analyses report their results using the {isoscalar,isovector} basis, such as XENON100, DEAP-3600, and PandaX-II [28–30], which prohibits direct comparison. However, we note that for xenon targets, the expected event rates for WIMP-n interactions are typically larger than that for WIMP-p interactions, but the isoscalar formulation splits the differences between these. Our WIMP-p limits are competitive (and sometimes more sensitive) than the isoscalar limits in Refs. [28, 29], indicating new exclusion of EFT WIMP parameter space, regardless of the chosen basis.

We also report the WS2014–16 inelastic scattering sensitivity limits excluding new EFT WIMP parameter space using the isoscalar basis. Figure 8 shows the inelastic EFT WIMP-nucleon isoscalar limits as a function of δ_m for a fixed WIMP mass of 1 TeV compared to the previous limits set by XENON100 [29]. At this mass we show similar limits to XENON100 despite using a larger exposure. This is due to overlap between our background models and signal models at higher energies; as we expect an increased amount of background in the signal region compared to traditional SI WIMP searches (due to $\gamma - X$ and ^{83m}Kr contamination), our expected upper-limits increase, reducing the impact of the larger exposure. Despite this, our 1 TeV inelastic limits are competitive with XENON100, and in some cases more sensitive. This effect is more severe for higher energies where the overlap between background and signal models is the largest; smaller mass WIMP models are not significantly effected by this reduction of sensitivity, however, we show the 1 TeV examples for the purpose of comparing to the existing XENON100 limits.

VII. SUMMARY

We have expanded and improved the LUX background models to allow for characterization of data at energies

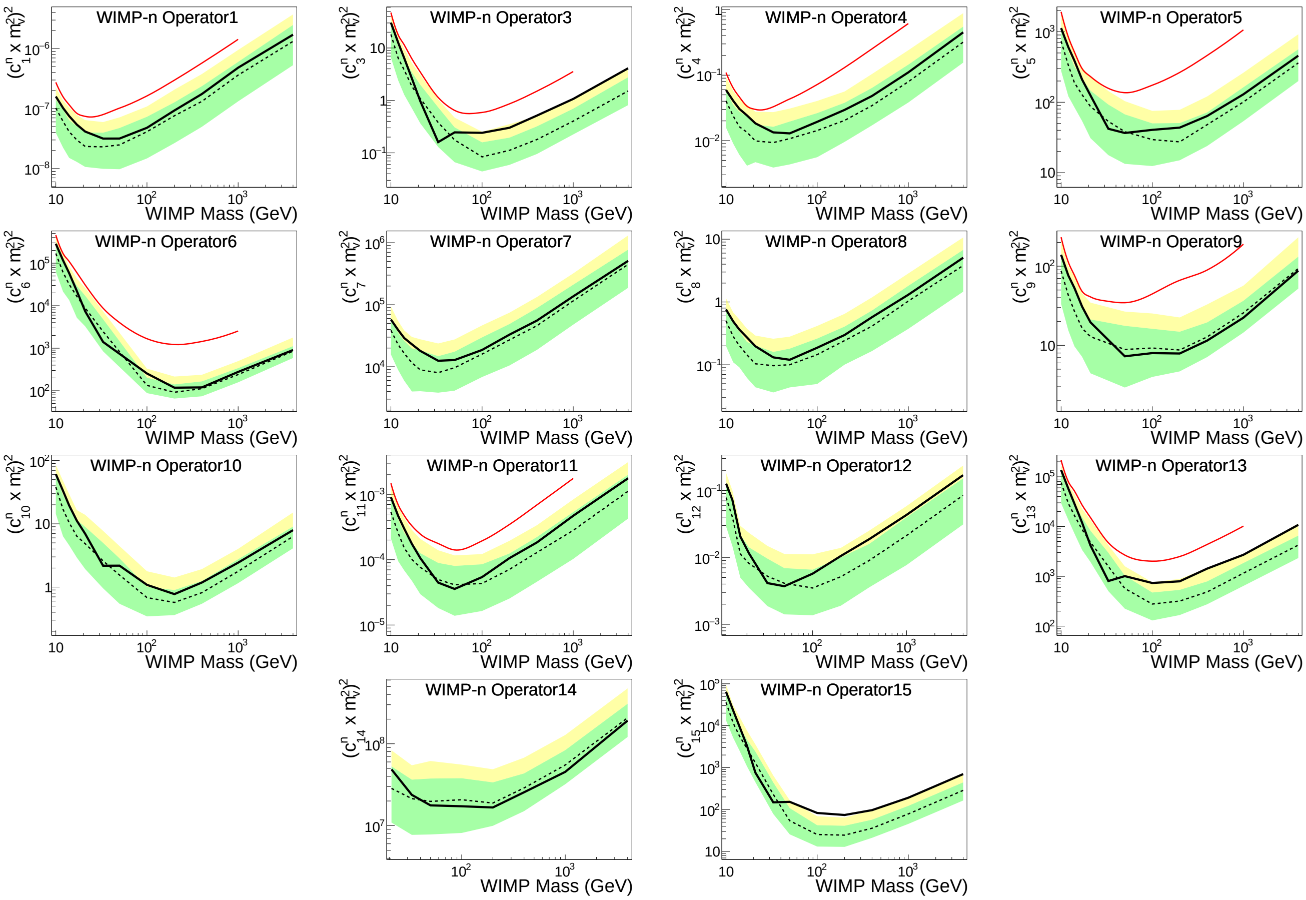

FIG. 6. The LUX WS2014–16 90% C.L. sensitivity limits for WIMP-neutron dimensionless couplings for each of the fourteen non-relativistic EFT operators. Solid black lines show the limit, while dashed black indicate the expectation, with green and yellow bands indicating the 1σ and 2σ sensitivity expectations, respectively. Each plot uses mass values of 10, 12, 14, 17, 21, 33, 50, 100, 200, 400, 1000, and 4000 GeV, except for Operators 12 and 14, which begin at 12 and 21 GeV, respectively. Red lines show the upper-limits from the WS2013 analysis [15].

much higher than a traditional WIMP search. These backgrounds include novel characterization of multiply-scattering $\gamma - X$ events disguised as single scatters, as well as the inclusion of $^{83\mathrm{m}}$Kr decays in our background model. Utilization of the Noble Element Simulation Technique allowed for efficient modeling of the ER and NR LXe response, independently for each of the 16 time and drift time bins of WS2014–16 data. Additionally, NEST allows us to extrapolate the NR LXe response to higher energies than measured with *in situ* calibrations, after accounting for the uncertainties in all of the light and charge yield measurements combined from beyond LUX.

We set exclusion limits for the 28 combinations of EFT operator and atomic nucleon in the {n, p} basis. While we consider this basis to be more physically intuitive, it does not allow for direct comparison with recent EFT WIMP sensitivity limits in the {isoscalar,isovector} basis.

We also report the results of inelastic WIMP-nucleon scattering with respect to isoscalar nucleons at 1 TeV and compare to those reported by the XENON100 Collaboration [29].

ACKNOWLEDGMENTS

This work was partially supported by the U.S. Department of Energy (DOE) under Award No. DE-AC02-05CH11231, DE-AC05-06OR23100, DE-AC52-07NA27344, DE-FG01-91ER40618, DE-FG02-08ER41549, DE-FG02-11ER41738, DE-FG02-91ER40674, DE-FG02-91ER40688, DE-FG02-95ER40917, DE-NA0000979, DE-SC0006605, DE-SC0010010, DE-SC0015535, and DE-SC0019066; the U.S. National Science Foundation under Grants No. PHY-0750671, PHY-0801536, PHY-1003660, PHY-1004661, PHY-1102470, PHY-1312561, PHY-1347449, PHY-1505868, and PHY-1636738; the Research Corporation Grant No. RA0350; the Center for Ultra-low Background Experiments in the Dakotas (CUBED); and the South Dakota School of Mines and Technology (SDSMT).

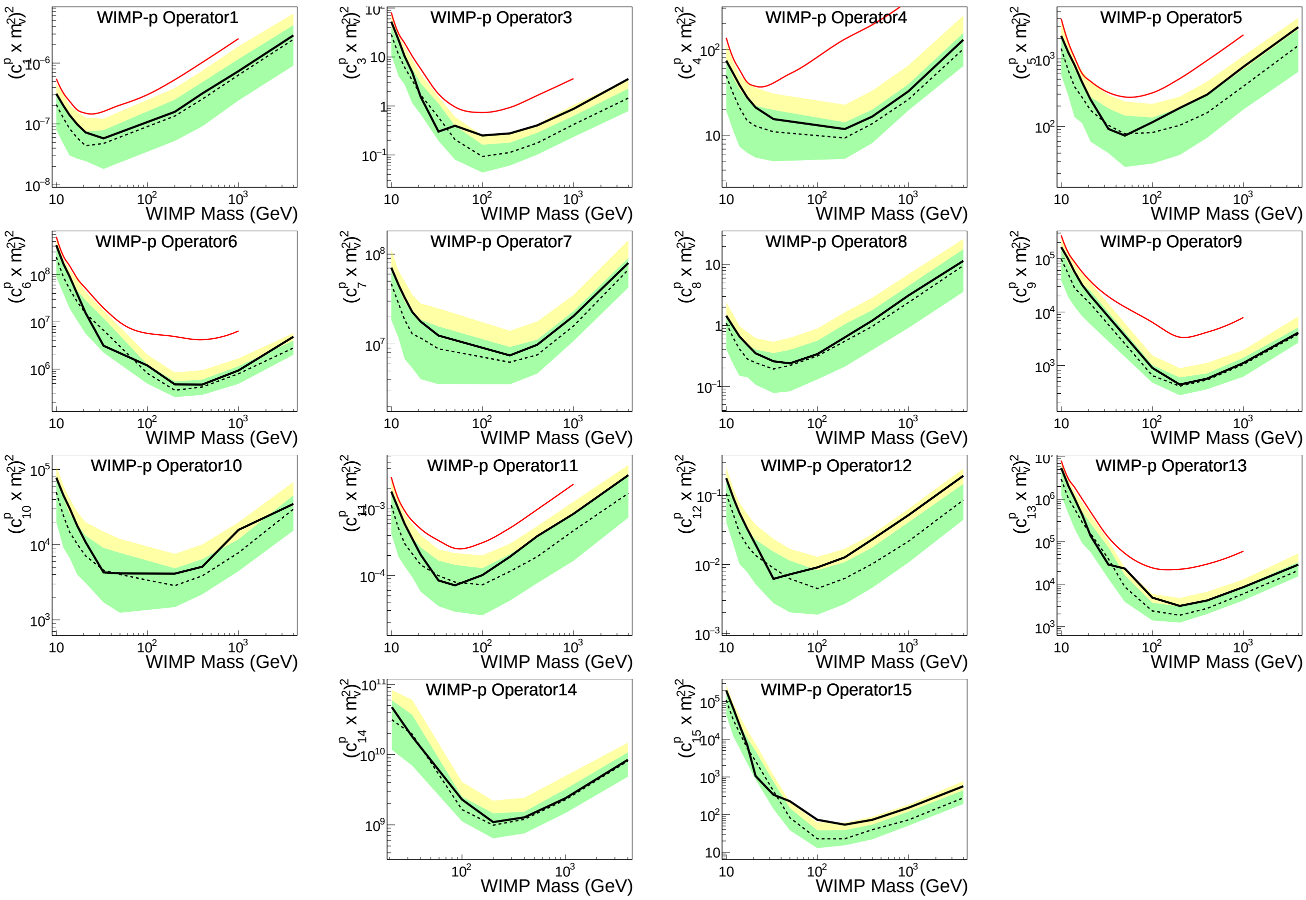

FIG. 7. The LUX WS2014–16 90% C.L. sensitivity limits for WIMP-proton dimensionless couplings for each of the fourteen non-relativistic EFT operators. Solid black lines show the limit, while dashed black indicate the expectation, with green and yellow bands indicating the 1σ and 2σ sensitivity expectations, respectively. Each plot uses mass values of 10, 12, 14, 21, 33, 50, 100, 200, 400, 1000, and 4000 GeV, with the exception of Operator 14, which begins at 21 GeV. Red lines show the upper-limits from the WS2013 analysis [15] .

Laboratório de Instrumentação e Física Experimental de Partículas (LIP)-Coimbra acknowledges funding from Fundação para a Ciência e a Tecnologia (FCT) through the Project-Grant PTDC/FIS-NUC/1525/2014. Imperial College and Brown University thank the UK Royal Society for travel funds under the International Exchange Scheme (IE120804). The UK groups acknowledge institutional support from Imperial College London, University College London and Edinburgh University, and from the Science & Technology Facilities Council for PhD studentships R504737 (EL), M126369B (NM), P006795 (AN), T93036D (RT) and N50449X (UU). This work was partially enabled by the University College London (UCL) Cosmoparticle Initiative. The University of Edinburgh is a charitable body, registered in Scotland, with Registration No. SC005336.

This research was conducted using computational resources and services at the Center for Computation and Visualization, Brown University, and also the Yale Science Research Software Core.

We gratefully acknowledge the logistical and technical support and the access to laboratory infrastructure provided to us by SURF and its personnel at Lead, South Dakota. SURF was developed by the South Dakota Science and Technology Authority, with an important philanthropic donation from T. Denny Sanford. SURF is a federally sponsored research facility under Award Number DE-SC0020216.

Appendix A: Illustration of Data Separation by Time and drift time bin

We present in this appendix the full WS2014–16 data used in this analysis, separated into the 16 drift time bins: four temporal bins, each subdivided to correspond to a 65 μs window of drift time. The livetimes for each temporal bin are: 43.9, 43.8, 85.8, and 137.7 days, respectively. Figure 9 illustrates the data compared to the relevant ER and NR simulated responses; bands represent 90% C.L. about the mean response. Despite the exclusion of exposures associated with the ^{83m}Kr calibration injections,

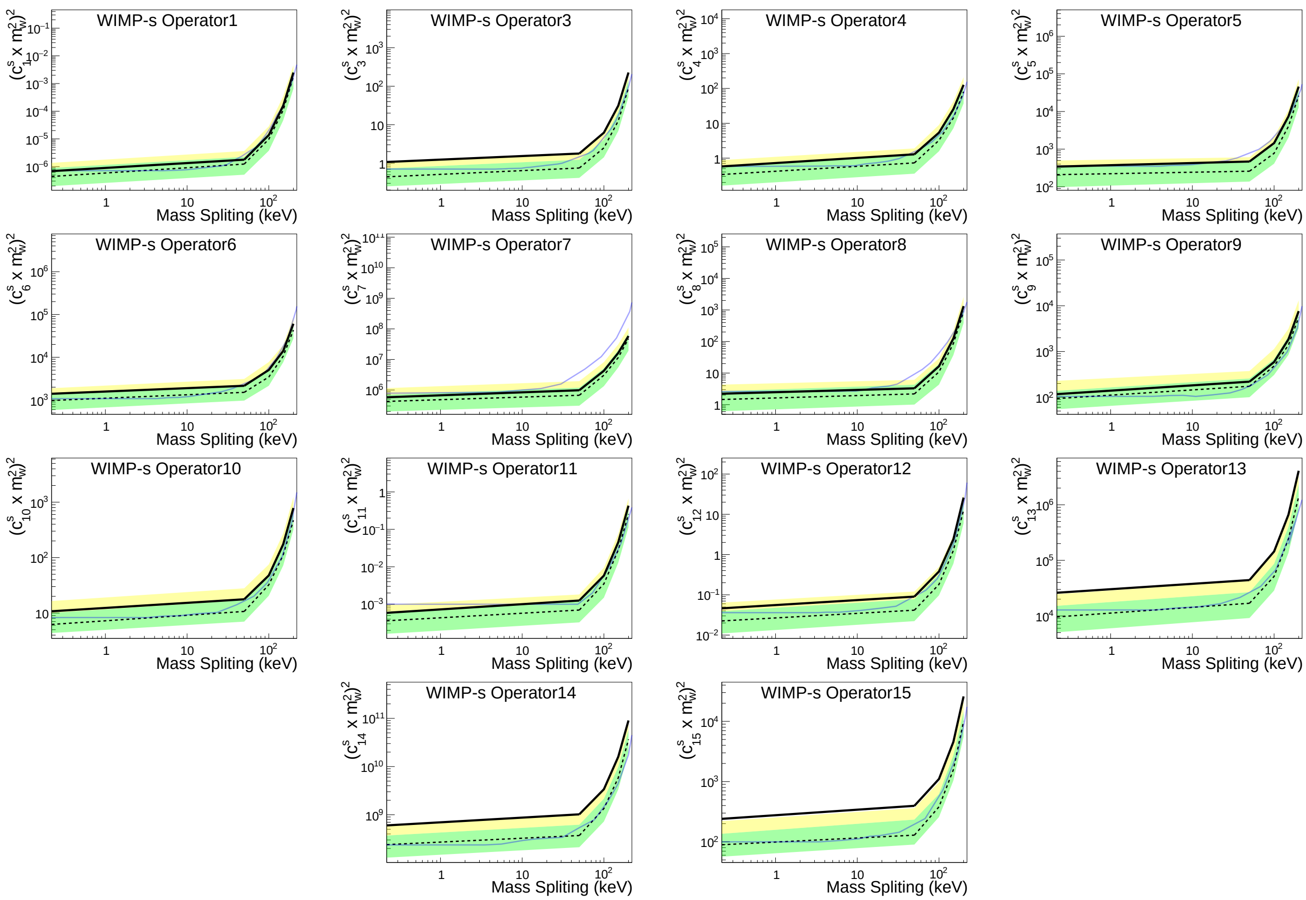

FIG. 8. The LUX WS2014–16 90% C.L. sensitivity limits for isoscalar WIMP-nucleon dimensionless couplings for each of the fourteen non-relativistic EFT operators and a fixed WIMP mass of 1 TeV. Solid black lines show the limit, while dashed black indicate the expectation, with green and yellow bands indicating the 1σ and 2σ sensitivity expectations, respectively. Each plot uses δ_m values of 0, 50, 100, 150, and 200 keV. Blue lines show limits from XENON100 [29].

many of these events can be seen in each drift time bin.

[1] V. Rubin and K. J. Ford, The Astrophysical Journal **159**, 379 (1970).

[2] D. Clowe, M. Bradac, A. H. Gonzalez, M. Markevitch, S. W. Randall, C. Jones, and D. Zaritsky, Astrophys. J. **648**, L109 (2006), arXiv:astro-ph/0608407 [astro-ph].

[3] L. Anderson *et al.* (BOSS), Mon. Not. Roy. Astron. Soc. **441**, 24 (2014), arXiv:1312.4877 [astro-ph.CO].

[4] R. Adam *et al.* (Planck), Astron. Astrophys. **594**, A1 (2016), arXiv:1502.01582 [astro-ph.CO].

[5] W. Hu and S. Dodelson, Ann. Rev. Astron. Astrophys. **40**, 171 (2002), arXiv:astro-ph/0110414 [astro-ph].

[6] J. L. Feng, Ann. Rev. Astron. Astrophys. **48**, 495 (2010), arXiv:1003.0904 [astro-ph.CO].

[7] D. S. Akerib *et al.* (LUX), Phys. Rev. Lett. **112**, 091303 (2014), arXiv:1310.8214 [astro-ph.CO].

[8] D. S. Akerib *et al.* (LUX), Phys. Rev. Lett. **118**, 021303 (2017), arXiv:1608.07648 [astro-ph.CO].

[9] D. S. Akerib *et al.* (LUX), Phys. Rev. Lett. **118**, 021303 (2017), arXiv:1608.07648 [astro-ph.CO].

[10] D. S. Akerib *et al.* (LUX), Phys. Rev. Lett. **118**, 251302 (2017), arXiv:1705.03380 [astro-ph.CO].

[11] E. Aprile *et al.*, Physical Review Letters **121** (2018), 10.1103/physrevlett.121.111302.

[12] X. Cui *et al.*, Physical Review Letters **119** (2017), 10.1103/physrevlett.119.181302.

[13] A. L. Fitzpatrick, W. Haxton, E. Katz, N. Lubbers, and Y. Xu, JCAP **1302**, 004 (2013), arXiv:1203.3542 [hep-ph].

[14] N. Anand, A. L. Fitzpatrick, and W. C. Haxton, Phys. Rev. **C89**, 065501 (2014), arXiv:1308.6288 [hep-ph].

[15] D. S. Akerib and others., "An effective field theory analysis of the first lux dark matter search," (2020), arXiv:2003.11141 [astro-ph.CO].

[16] D. Akerib *et al.*, Physical Review D **96** (2017), 10.1103/physrevd.96.112009.

[17] D. Akerib *et al.*, Journal of Instrumentation **15**, T02007–T02007 (2020).

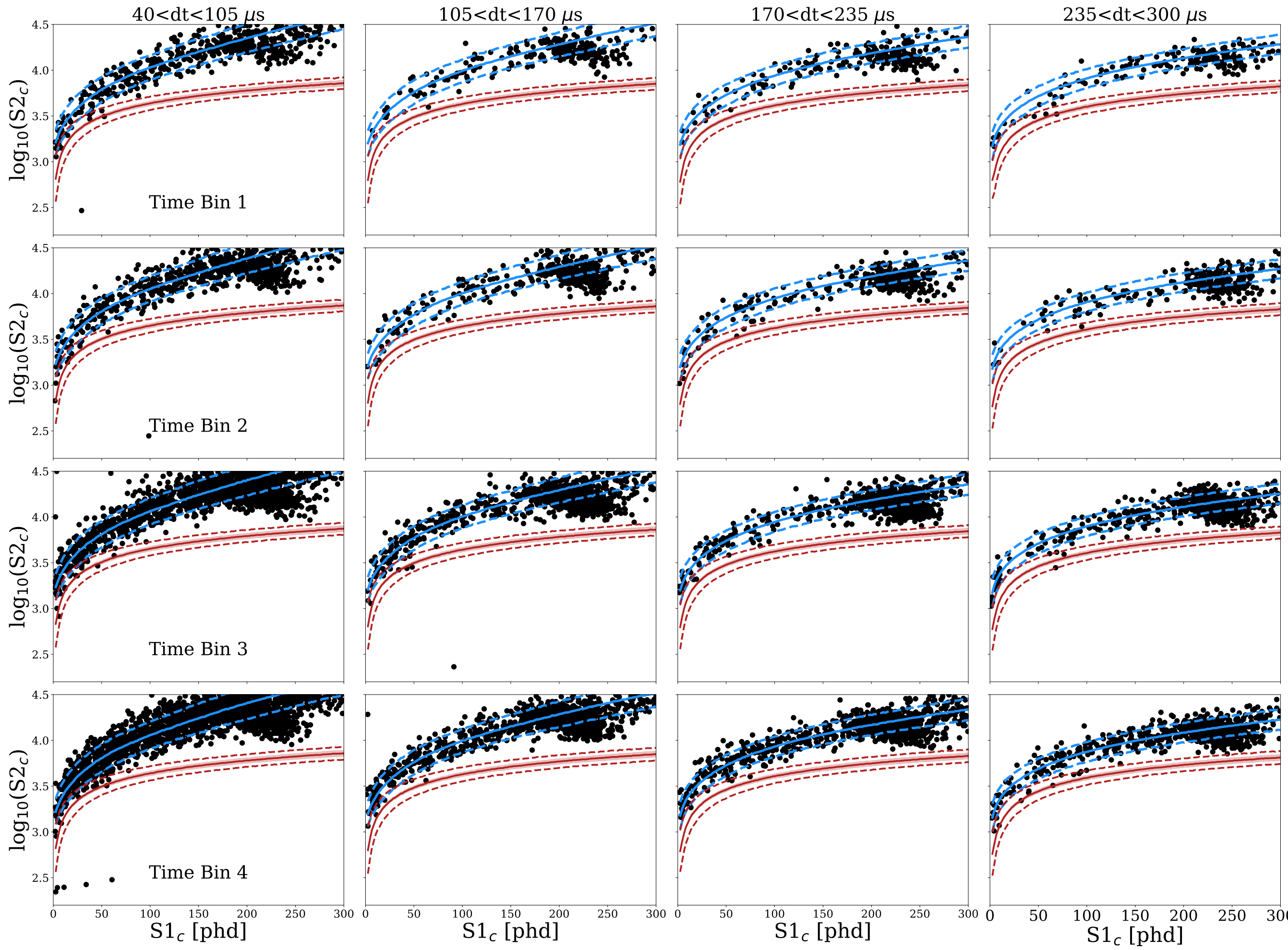

FIG. 9. The WS2014–16 data divided into the 16 drift time bins: four temporal bins of unequal livetime subdivided further into four spatial bins. Blue bands represent the mean and 90% C.L. ER response, while red illustrates the mean and 90% C.L. NR response. 20.8 live-days of data corresponding to significant ^{83m}Kr contamination have been removed from this data set, however, remaining ^{83m}Kr events can be seen encroaching upon the signal region at higher energies.

[18] D. Akerib *et al.*, Physical Review D **93** (2016), 10.1103/physrevd.93.072009.
[19] D. Akerib *et al.*, Physical Review D **100** (2019), 10.1103/physrevd.100.022002.
[20] D. S. Akerib *et al.* (LUX), (2016), arXiv:1608.05381 [physics.ins-det].
[21] "Multiphysics software for optimizing designs," https://www.comsol.com/.
[22] D. Akerib *et al.*, Journal of Instrumentation **12**, P11022–P11022 (2017).
[23] D. Akerib *et al.*, Physical Review D **102** (2020), 10.1103/physrevd.102.112002.
[24] D. Akerib *et al.*, Physical Review D **98** (2018), 10.1103/physrevd.98.062005.
[25] D. Akerib *et al.*, Physical Review D **102** (2020), 10.1103/physrevd.102.092004.
[26] D. Akerib *et al.*, "Improving sensitivity to low-mass dark matter in lux using a novel electrode background mitigation technique," (2020), arXiv:2011.09602 [hep-ex].
[27] Y. Coadou, EPJ Web of Conferences **55**, 02004 (2013).
[28] P. Adhikari *et al.*, Physical Review D **102** (2020), 10.1103/physrevd.102.082001.
[29] E. Aprile *et al.*, Physical Review D **96** (2017), 10.1103/physrevd.96.042004.
[30] J. Xia *et al.* (PandaX), arXiv:1807.01936 [hep-ex].
[31] M. Szydagis, J. Balajthy, J. Brodsky, J. Cutter, J. Huang, E. Kozlova, B. Lenardo, A. Manalaysay, D. McKinsey, M. Mooney, J. Mueller, K. Ni, G. Rischbieter, M. Tripathi, C. Tunnell, V. Velan, and Z. Zhao, "Noble element simulation technique," (2020).
[32] P. Sorensen and C. E. Dahl, Physical Review D **83** (2011), 10.1103/physrevd.83.063501.
[33] G. Barello, S. Chang, and C. A. Newby, Physical Review D **90** (2014), 10.1103/physrevd.90.094027.
[34] D. Akerib *et al.*, Physical Review Letters **116** (2016), 10.1103/physrevlett.116.161301.
[35] D. Akerib *et al.*, Journal of Instrumentation **13**, P02001–P02001 (2018).
[36] E. Aprile *et al.*, Physical Review D **99** (2019), 10.1103/physrevd.99.112009.
[37] J. Neyman, Phil. Trans. R. Soc. Lond. A **236**, 333 (1937).
[38] G. Cowan, K. Cranmer, E. Gross, and O. Vitells, The European Physical Journal C **71** (2011), 10.1140/epjc/s10052-011-1554-0.

[39] W. Verkerke and D. Kirkby, (2003), 10.1142/9781860948985_0039.

[40] K. Schneck, B. Cabrera, D. Cerdeño, V. Mandic, H. Rogers, R. Agnese, A. Anderson, M. Asai, D. Balakishiyeva, D. Barker, , *et al.*, Physical Review D **91** (2015), 10.1103/physrevd.91.092004.